

# Modeling of power transmission and stress grading for corona protection

T. I. Zohdi<sup>1</sup> · B. E. Abali<sup>1</sup> 

Received: 1 July 2017 / Accepted: 26 October 2017  
© Springer-Verlag GmbH Germany, part of Springer Nature 2017

**Abstract** Electrical high voltage (HV) machines are prone to corona discharges leading to power losses as well as damage of the insulating layer. Many different techniques are applied as corona protection and computational methods aid to select the best design. In this paper we develop a reduced-order model in 1D estimating electric field and temperature distribution of a conductor wrapped with different layers, as usual for HV-machines. Many assumptions and simplifications are undertaken for this 1D model, therefore, we compare its results to a direct numerical simulation in 3D quantitatively. Both models are transient and nonlinear, giving a possibility to quickly estimate in 1D or fully compute in 3D by a computational cost. Such tools enable understanding, evaluation, and optimization of corona shielding systems for multilayered coils.

**Keywords** Finite element · Electromagnetism · Corona protection · Temperature · Reduced order model

## 1 Introduction

With the invention of power transformer in 1880s, the feasibility of power transmission was greatly increased. Growing demand in electric power motivates researchers for further optimization in power transmission. High voltage (HV) machines generate electric current transported in specially designed cables as alternate current (AC) or direct current (DC). These HVAC or HVDC transmission mediums have several inefficiencies leading to losses and leakage, which

imply an active research and development, see [8,21,23]. Two important issues for HVAC as well HVDC are: high amount of heat produced by the electric current and power loss due to a corona discharge. These phenomena are also related to each other, since the produced heat increases the temperature of the surrounding air, which enhances the ionization leading to corona. The cables are insulated, for example with resin like polypropylene or with a high-dense Kraft paper, and along the surface of this insulation the electric potential varies. If the potential gradient exceeds a material specific threshold value, coronas break down the surface of insulating layer. Therefore, an extra layer is used as corona protection by equalizing the potential gradient.

Corona protection is realized by using a partially-insulating layer wrapped around the insulating layer surrounding the conducting core (copper). Silicon carbide filled resin or inorganic fiber reinforced composite material is used as a semiconductor around the insulator, see [7,17,18] and the references in [34]. Such a material is more efficient as a thermal conductor and also its electrical resistivity increases with an increasing applied electric field (voltage stress),  $E$ . This corona protection layer can be applied as a lacquer (paint, spray) or tape (band). As outer corona protection or shielding (OCP or OCS), a slightly different coating is used than as end corona protection or shielding (ECP or ECS) along the wire. These different materials used for corona protection are called *stress grading* materials—we use the wording *electric field* instead of *voltage stress*. Such materials are semiconductors; hence, the resistivity depends on temperature as well as on electric field, see [11,31].

Different proposals have been used for simulating the system response of power transmission. MAXWELL's equations coupled with the balance of energy need to be solved in order to obtain distribution of electromagnetic fields and temperature in the system. With system specific assumptions and

✉ B. E. Abali  
bilanemek@abali.org

<sup>1</sup> Department of Mechanical Engineering, University of California, Berkeley, Berkeley, CA, USA

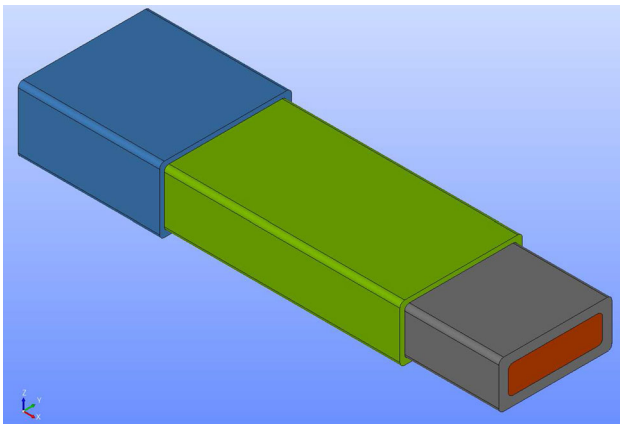


**Fig. 1** Power transmission cable model, copper as core (orange), resin as insulator (gray), OCP (green), and ECP (blue). (Color figure online)

simplifications, numerical solutions are presented by several researchers, see [12, 13, 25–30].

In this work we propose an efficient reduced-order model in 1D and test its accuracy by using a transient solution of coupled field equations based on finite element method (FEM) in 3D. As a model we use 10 cm × 3 cm copper block of 50 cm length, covered with a resin of 1 cm thickness. We decompose it into 3 sections of 10-30-10 cm and use at first and second sections OCP and at first section ECP, both 0.5 cm of thickness. All corners are filled with 0.5 cm of radius. The geometry can be depicted in Fig. 1.

## 2 Field equations for 1D model problem

The continuum body is modeled as a rigid, unpolarized, and conductive system. Therefore, we need to solve two coupled field equations for computing the electric potential  $V$  and the temperature  $\theta$ . We explain for the one-dimensional sys-

an electric charge enters a control volume, another electric charge leaves the control volume such that the total amount of charge remains conserved. It reads

$$+(JA)^- - (JA)^+ = 0 \tag{1}$$

along  $\Delta x$  and if  $\Delta x \rightarrow 0$ , by using OHM’s law,  $J = \sigma E$ , we obtain

$$\frac{d(JA)}{dx} = \frac{d(\sigma EA)}{dx} = 0, \tag{2}$$

where  $A(x)$  is the cross-sectional area, which changes section by section as seen in Fig. 1. The flow of current can be rewritten by using,  $E = -dV/dx$  as follows

$$\frac{d(JA)}{dx} = \frac{d(\sigma EA)}{dx} = -\frac{d}{dx} \left( \sigma \frac{dV}{dx} A \right) = 0, \tag{3}$$

where the voltage is controlled at the ends  $V(x = 0) = V_0$  and  $V(x = L) = V_L$ . Hence Eq. 3 is solved as

$$\begin{aligned} \sigma \frac{dV}{dx} A &= c_1, \\ V - V_0 &= c_1 \int_0^x \frac{d\bar{x}}{\sigma(\bar{x}, t)A(\bar{x})}, \\ V(x, t) &= V_0 + \frac{V_L - V_0}{\int_0^L \frac{d\bar{x}}{\sigma(\bar{x}, t)A(\bar{x})}} \int_0^x \frac{d\bar{x}}{\sigma(\bar{x}, t)A(\bar{x})}. \end{aligned} \tag{4}$$

We can simply evaluate for every  $x$  by providing the conductivity  $\sigma$  as well as the cross-sectional area  $A$  for every section. Concretely, for a beam of 3 sections with lengths  $L^I, L^{II}, L^{III}$ , such that  $L = L^I + L^{II} + L^{III}$  we have

$$\int_0^L \frac{d\bar{x}}{\sigma(\bar{x}, t)A(\bar{x})} = \frac{L^I}{\sigma^I A^I} + \frac{L^{II}}{\sigma^{II} A^{II}} + \frac{L^{III}}{\sigma^{III} A^{III}},$$

$$\int_0^x \frac{d\bar{x}}{\sigma(\bar{x}, t)A(\bar{x})} = \begin{cases} \frac{x}{\sigma^I A^I} & \text{if } x < L^I \\ \frac{L^I}{\sigma^I A^I} + \frac{x - L^I}{\sigma^{II} A^{II}} & \text{if } x \geq L^I \text{ and } x < L^I + L^{II} \\ \frac{L^I}{\sigma^I A^I} + \frac{L^{II}}{\sigma^{II} A^{II}} + \frac{x - (L^I + L^{II})}{\sigma^{III} A^{III}} & \text{if } x \geq L^I + L^{II} \end{cases} \tag{5}$$

tem under consideration, a simple but reliable semi-analytic method in order to determine  $V$  and  $\theta$  quickly.

### 2.1 Current flow

Signal propagation is fast with respect to the motion of electric charge. Hence it is appropriate to assume that at the time

Every section consists of different layers. The copper core is framed with different layers such as insulator, ECP, OCP. For a section  $\alpha \in \{I, II, III\}$  suppose there are  $n \in \{1, 2, 3, 4, \dots\}$  layers of different materials. Every layer has an electrical conductivity  $\sigma_n$  and a corresponding cross-section area  $A_n$ . Since the electric field is assumed uniform at each cross-section (at a fixed location  $x$ ), the electric current area density,

$\sigma(x, t)E$ , over the whole cross-section reads

$$\frac{1}{A(x)} \int_{A(x)} J \, dA = \frac{1}{A(x)} \sum_{i=1}^n J_i A_i = \frac{1}{A(x)} \sum_{i=1}^n \sigma_i E A_i. \tag{6}$$

Thus, we obtain

$$\sigma(x, t) = \frac{1}{A(x)} \sum_{i=1}^n \sigma_i A_i. \tag{7}$$

The effective conductivity of a cross-section is the sum of the individual conductivities multiplied by their share of the cross-sectional area. In each section we have

$$\sigma^\alpha = \frac{1}{A^\alpha} \sum_{i=1}^n \sigma_i^\alpha A_i^\alpha, \quad A^\alpha = \sum_{i=1}^n A_i^\alpha. \tag{8}$$

In each section, the number of layers may vary,  $n = n(\alpha)$ , which we have omitted in the notation for the sake of brevity.

### 2.2 Temperature evolution

Analogously, we use the energy conservation within a control volume

$$\rho c \frac{\partial \theta}{\partial t} \Delta V = +(qA)^- - (qA)^+ + aJE \Delta V, \tag{9}$$

where the volume is  $\Delta V = A \Delta x$ ,  $c$  denotes the (constant in each section) specific heat capacity,  $q = -\kappa \partial \theta / \partial x$  is the heat flux, and a system specific parameter  $a$  models possible losses from the control volume, we set  $a = 1$ . Dividing both sides by  $\rho c \Delta V$  yields

$$\frac{\partial \theta}{\partial t} = \underbrace{\frac{1}{\rho c} \frac{\partial}{\partial x} \left( \kappa \frac{\partial \theta}{\partial x} \right)}_{\mathcal{F}(x, t)} + \frac{JE}{\rho c}. \tag{10}$$

Approximating the time derivative of  $\theta$  at  $x$  and  $t$  as

$$\frac{\partial \theta}{\partial t} \approx \frac{\theta(x, t + \Delta t) - \theta(x, t)}{\Delta t} \tag{11}$$

we obtain

$$\theta(x, t + \Delta t) = \theta(x, t) + \Delta t \mathcal{F}(x, t). \tag{12}$$

For the derivative term inside of  $\mathcal{F}$ , we approximate

$$\frac{\partial}{\partial x} \left( \kappa \frac{\partial \theta}{\partial x} \right) = \frac{\partial}{\partial x} \left( \frac{\kappa(x)}{\Delta x} \left( \theta \left( x + \frac{\Delta x}{2} \right) - \theta \left( x - \frac{\Delta x}{2} \right) \right) \right)$$

$$= \frac{1}{(\Delta x)^2} \left( \kappa \left( x + \frac{\Delta x}{2} \right) \left( \theta \left( x + \Delta x \right) - \theta \left( x \right) \right) - \kappa \left( x - \frac{\Delta x}{2} \right) \left( \theta \left( x \right) - \theta \left( x - \Delta x \right) \right) \right). \tag{13}$$

### 2.3 Algorithm

The solution algorithm for the reduced-order model works in 1D. The geometry consists of different parts (layers) such as copper, resin, ECP, and OCP. These layers have different material properties used for calculating the effective conductivity. In the 1D model we compute electric potential and temperature only within the copper core; however, we present the results on a 3D mesh for the sake of a better visualization.

A line mesh is generated and along that line the electric potential is computed with Eq. (4) by using the temperature field from the last time step. Since we have neglected polarization, the electric potential is identical for different layers. Therefore, we can solve for the whole body with one reduced 1D model. After the computation of the electric potential, the temperature distribution is computed with Eq. (12) by using the current electric potential. Since JOULE’s heat depends on the material coefficient (electrical conductivity), for each of the layer we need to determine the temperature separately as another 1D model. So in each time step we follow the steps:

- Compute the electric potential  $V$  along  $x$  by using the temperature from the last time step  $\theta^0$  (or initial condition),
- Compute  $J$  and  $E$  with the current value of  $\sigma$  in each layer,
- Compute  $\theta(x, t + \Delta t)$  at each node in system,
- Compute  $\sigma^*(x, t + \Delta t)$ , go to the next time step and repeat.

We solve two 1D equations: one for electric potential and another for temperature. Then we derive electric field and electric current from the solution and combine them in a 3D mesh for a better visualization. The computation is fast; but it may be error prone effected by the various assumptions. First, we assume rigid bodies and neglect dielectric properties of the materials (no polarization). Second, we use a weak coupling in the sense that the temperature and the electric field affect each other with a delay of one time step. Third, we neglect the magnetic potential completely. Fourth, the heat flux is only along  $x_1$  and we ignore a heat exchange with the environment (no losses). These assumptions might lead to inaccuracies. In order to estimate the accuracy of this reduced model, we implement a direct numerical computation in 3D and compare the results of 1D to the results in 3D.

### 3 Direct numerical FEM calculations

Consider a rigid, polarized continuum body, within which we want to compute the electric potential  $\phi$ , the magnetic potential  $A$ , and the temperature  $T$  as a function in space  $x$  and in time  $t$ . We call the list unknowns  $\{\phi, A, T\}$  as the primitive variables. The solution of primitive variables has to fulfill the governing equations motivated by balance equations. We very briefly sum up this motivation and present the governing equations, for details we refer to [2, Chap. 3]. All fields are expressed in Cartesian coordinates, we apply EINSTEIN’s summation convention over repeated indices, and we understand a derivative with respect to  $x_i$  by the comma notation  $(\cdot)_{,i}$  as a lower index.

The continuum body has an electric charge composed of free and bound charges. Their characteristics differ since the free charges move in macroscopic distances, whereas the bound charges displace in microscopic lengths. We start with the balance of electric charge as well as balance of magnetic flux such that four MAXWELL equations are derived. Two of them can be solved by means of the following *ansatz* functions

$$E_i = -\phi_{,i} - \frac{\partial A_i}{\partial t}, \quad B_i = \epsilon_{ijk} A_{k,j}, \tag{14}$$

between electromagnetic fields  $E_i, B_i$  and electromagnetic potentials  $\phi, A_i$  up to an arbitrary gauge—because of numerical reasons, we apply the LORENZ gauge. By starting with the balance of electric charge and inserting MAXWELL’s equations, we obtain

$$\frac{\partial \mathfrak{D}_{i,i}}{\partial t} + \left( J_i^{\text{fr.}} + \epsilon_{ijk} \mathcal{M}_{k,j} \right)_{,i} = 0, \tag{15}$$

where the charge potential  $\mathfrak{D}_i$  (also called the dielectric displacement) is created by the free electric charges,  $J_i^{\text{fr.}}$  denotes the electric current due to the motion of the free electric charges,  $\epsilon_{ijk}$  is the LEVI-CIVITA symbol being equal to the permutation symbol in Cartesian coordinates, and the magnetic polarization  $\mathcal{M}_i$  is the magnetization effected by the bound electric charges. In the case of a rigid body, for  $\mathfrak{D}_i, J_i^{\text{fr.}}$ , and  $\mathcal{M}_i$  we apply following constitutive equations:

$$\begin{aligned} \mathfrak{D}_i &= D_i + P_i, \quad D_i = \epsilon_0 E_i, \quad P_i = \epsilon_0 \chi^{\text{el.}} E_i, \\ J_i^{\text{fr.}} &= \sigma \pi T_{,i} + \sigma E_i, \quad \mathcal{M}_i = \frac{\chi^{\text{mag.}}}{\mu_0(1 + \chi^{\text{mag.}})} B_i, \end{aligned} \tag{16}$$

giving the connection to the electric field  $E_i$ , the magnetic flux  $B_i$ , and the temperature  $T$  by means of the universal constants  $\epsilon_0$  and  $\mu_0$ , as well as the material specific coefficients, namely the electrical conductivity  $\sigma$ , thermoelectric or PELTIER’s constant  $\pi$ , electric susceptibility  $\chi^{\text{el.}}$ , and magnetic susceptibility  $\chi^{\text{mag.}}$ . Electric polarization  $P_i$  is due to

the bound electric charges. Herein we neglect the magneto-electric effect such that electric polarization depends only on the electric field, analogously, magnetic polarization depends only on the magnetic flux. For computing the magnetic potential,  $A_i$ , we utilize MAXWELL’s equation and after inserting the LORENZ gauge, we acquire

$$\epsilon_0 \frac{\partial^2 A_i}{\partial t^2} - \frac{1}{\mu_0} A_{i,jj} = J_i^{\text{fr.}} + \frac{\partial P_i}{\partial t} + \epsilon_{ijk} \mathcal{M}_{k,j}. \tag{17}$$

For computing the temperature  $T$ , we use the balance of entropy

$$\rho \frac{\partial \eta}{\partial t} + \Phi_{i,i} - \rho \frac{r}{T} = \Sigma, \tag{18}$$

where the supply term  $r$  vanishes in our application, the specific (per mass) entropy  $\eta$  and its flux  $\Phi_i$  as constitutive equations and the production term  $\Sigma$  read

$$\begin{aligned} \eta &= c \ln \left( \frac{T}{T_{\text{ref.}}} \right), \quad \Phi_i = \frac{q_i}{T}, \quad q_i = -\kappa T_{,i} + \sigma \pi T E_i, \\ \Sigma &= -\frac{q_i}{T^2} T_{,i} + \frac{1}{T} E_i J_i^{\text{fr.}}, \end{aligned} \tag{19}$$

for rigid, polarized, thermal bodies under the assumption that irreversible polarization effects (such as hysteresis) are neglected. The additional material coefficients—specific heat capacity  $c$ , thermal conductivity  $\kappa$ —need to be determined for every different material by means of experiments.

The governing Eqs. (15), (17), (18) are coupled and non-linear. In order to solve them we use finite element method in space and finite difference method in time. For the space discretization we follow the standard variational formulation, namely multiply the governing equations with appropriate test functions and integrate by parts for weakening the continuity condition. The 5 primitive variables  $\mathbf{p} = \{\phi, A_1, A_2, A_3, T\}$  are approximated as a class  $C^n$  function in 5-dimensional HILBERT space,

$$\mathcal{V} = \left\{ \mathbf{p} \in [\mathcal{H}^n(\Omega)]^5 : \mathbf{p}|_{\partial\Omega} = \text{given} \right\}, \tag{20}$$

where the differentiability properties are included such that it is a SOBOLEV space. For the sake of simplicity, we omit to emphasize the discrete representations of the analytic functions and use the same symbols henceforth. Furthermore, we use the GALERKIN approach and choose test functions from the same space as the primitive variables, whereas the test functions vanish on the DIRICHLET boundaries. For the time discretization, we choose the EULER backwards schema. After space and time discretization, we acquire the following weak forms:

$$F_\phi = \int_\Omega \left( -(\mathfrak{D}_i - \mathfrak{D}_i^0) \delta \phi_{,i} - \Delta t J_i^{\text{fr.}} \delta \phi_{,i} - \Delta t \epsilon_{ijk} \mathcal{M}_{k,j} \delta \phi_{,i} \right) dv$$

$$\begin{aligned}
 & + \int_{\partial\Omega} n_i \Delta t \epsilon_{ijk} \llbracket \mathcal{M}_{k,j} \rrbracket \delta\phi da, \\
 F_A = & \int_{\Omega} \left( \epsilon_0 \frac{A_i - 2A_i^0 + A_i^{00}}{\Delta t^2} \delta A_i + \frac{1}{\mu_0} A_{i,j} \delta A_{i,j} - J_i^{\text{fr}} \delta A_i \right. \\
 & \left. - \frac{P_i - P_i^0}{\Delta t} \delta A_i + \epsilon_{ijk} \mathcal{M}_k \delta A_{i,j} \right) dv, \\
 F_T = & \int_{\Omega} \left( \rho(\eta - \eta^0) \delta T - \Delta t \Phi_i \delta T_{,i} - \Delta t \rho \frac{r}{T} \delta T - \Delta t \Sigma \delta T \right) dv \\
 & + \int_{\partial\Omega} \Delta t \llbracket \Phi_i \rrbracket \delta T n_i da. \tag{21}
 \end{aligned}$$

We solve in discrete time steps. Terms with an upper index of zero,  $(\cdot)^0$ , denote the numerical values from the last time step. The jump brackets,  $\llbracket(\cdot)\rrbracket$ , indicate the difference on a surface between the values determined by the shape functions of adjacent (neighboring) finite elements. The solution fields, namely  $\phi$ ,  $A_i$ , and  $T$  are continuous over the element boundaries; however, the constitutive equations may have jumps across the interface between two different materials. We already applied the well-known jump conditions over the element boundaries by assuming that no surface charges and currents are existing and assuming that the electric current is continuous (along the normal direction  $n_i$ ), see [4] for details. Assembly over the whole domain give the nonlinear and coupled weak form

$$\text{Form} = F_{\phi} + F_A + F_T, \tag{22}$$

which is solved after an automatic linearization at the partial differential level by using the novel collection of packages developed under the FEniCS project [16,20]. It is important to distinguish the method used herein from the rich literature for computation of electromagnetism. We use standard finite elements of order one, which is not used for electromagnetism. Starting with [24] and [22], solution of MAXWELL’s equation are obtained by using mixed elements, for different proposals and implementations, see [6,9], [10, Sect. 17], [14, 19]. Nowadays, there exist several element types, see [5]. Roughly, the overall idea relies on solving electromagnetic fields,  $E_i$  and  $B_i$ , by satisfying all MAXWELL equations. Of course, this strategy is fine; however, by using electromagnetic potentials,  $\phi$  and  $A_i$ , it is possible to solve the system by means of standard finite elements, as presented in [2, Chap. 3], [3,4] with various examples. We use the same element type, namely  $\mathcal{P}_1$  continuous LAGRANGE elements of order one for each primitive variable.

### 4 Material properties

As electrical conductor, nearly always, copper is used, which is a homogeneous and isotropic material at least in the millimeter length-scale. The copper core is surrounded by an

insulator in order to avoid arcing. A polymeric type of resin will be modeled. ECP and OCP are particle-functionalized or fiber reinforced composite materials. Owing to the nature of composite character, we need to introduce estimates on the material properties. For every constitutive equation for OCP and ECP, we use “effective” material constants

$$\begin{aligned}
 \langle P_i \rangle_{\Omega} &= \epsilon_0 \chi_{\text{el}}^* \langle E_i \rangle_{\Omega}, \\
 \langle \mathcal{M}_i \rangle_{\Omega} &= \frac{\chi_{\text{mag.}}}{\mu_0(1 + \chi_{\text{mag.}}^*)} \langle B_i \rangle_{\Omega}, \\
 \langle J_i^{\text{fr}} \rangle_{\Omega} &= -\sigma^* \pi^* \langle T_{,i} \rangle_{\Omega} + \sigma^* \langle E_i \rangle_{\Omega}, \\
 \langle q_i \rangle_{\Omega} &= -\kappa^* \langle T_{,i} \rangle_{\Omega} + \sigma^* \pi^* \langle T \rangle_{\Omega} \langle E_i \rangle_{\Omega}, \tag{23}
 \end{aligned}$$

where  $(\cdot)^*$  is the effective material parameter of the composite material,  $\langle \cdot \rangle_{\Omega}$  is the volume averaged field with the averaging operator:

$$\langle \cdot \rangle_{\Omega} \stackrel{\text{def}}{=} \frac{1}{|\Omega|} \int_{\Omega} (\cdot) d\Omega \tag{24}$$

over a statistically representative volume element with domain  $\Omega$ . In the following we briefly present how to estimate the effective parameters based on [32,33].

#### 4.1 Determining the effective material parameters

In order to make estimates of the overall properties of the composite, we consider the widely used HASHIN–SHTRIKMAN bounds for isotropic materials with isotropic effective responses. These estimates provide one with upper and lower bounds on the overall response of the material. For two isotropic materials with an overall isotropic response, we utilize the following estimates:

$$\underbrace{\sigma_1 + \frac{v_2}{\frac{1}{\sigma_2 - \sigma_1} + \frac{1 - v_2}{3\sigma_1}}}_{\sigma^{*,-}} \leq \sigma^* \leq \underbrace{\sigma_2 + \frac{1 - v_2}{\frac{1}{\sigma_1 - \sigma_2} + \frac{v_2}{3\sigma_2}}}_{\sigma^{*,+}}, \tag{25}$$

where the conductivity of phase 2 (with volume fraction  $v_2$ ) is larger than phase 1 ( $\sigma_2 \geq \sigma_1$ ). Usually,  $v_2$  corresponds to the particle material, although there can be applications where the matrix is more conductive than the particles. In that case,  $v_2$  would correspond to the matrix material. Provided that the volume fractions and constituent conductivities are the only known information about the microstructure, the expressions are the tightest bounds for the overall isotropic effective responses for two phase media, where the constituents are both isotropic. A critical observation is that the lower bound is more accurate when the material is composed of high conductivity particles that are surrounded by a low conductivity matrix (denoted case 1) and the upper bound is more accurate

for a high conductivity matrix surrounding low conductivity particles (denoted case 2).

This can be explained by considering two cases of material combinations, one with 50% low conductivity material and 50% high conductivity material. A material with a continuous low conductivity (fine-scale powder) binder (50%) will isolate the high conductivity particles ((50%), and the overall system will not conduct electricity well (this is case 1 and the lower bound is more accurate), while a material formed by a continuous high conductivity (fine-scale powder) binder (50%) surrounding low conductivity particles (50%, case 2) will, in an overall sense, conduct electricity better than case 1. Thus, case 2 is more closely approximated by the upper bound and case 1 is closer to the lower bound. Since the true effective property lies between the upper and lower bounds, one can construct the following approximation

$$\sigma^* \approx \Psi \sigma^{*,+} + (1 - \Psi) \sigma^{*,-}, \tag{26}$$

where  $0 \leq \Psi \leq 1$  depends on the microstructure and must be calibrated. For high conductivity spherical particles, at low volume fractions, under 15%, where the particles are not in contact, the lower bound is more accurate. Thus, one would pick  $\Psi = \Psi^s \leq 0.5$  to bias the estimate to the lower bound. However, using the same setup but replacing the spherical particles with flakes, there is a greater likelihood of connecting flakes, thus producing high-conductivity pathways. Their overall conductivity will be higher than those of sphere at the same volume fraction. Thus, one would pick  $\Psi = \Psi^f > \Psi^s$ . One can calibrate  $\Psi$  by comparing it to different experiments as already done in [35]. Essentially, more particle interaction makes the upper bound more relevant. The general trends are (a) for cases where the upper bound is more accurate,  $\Psi > \frac{1}{2}$  and (b) for cases when the lower bound is more accurate,  $\Psi < \frac{1}{2}$ . The parameter  $\Psi$  indicates the degree of interaction of the particulate constituents. Analogously, the thermal conductivity has the following bounds

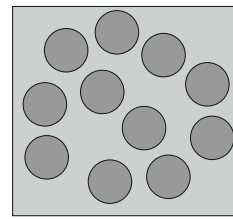
$$\underbrace{\kappa_1 + \frac{v_2}{\frac{1}{\kappa_2 - \kappa_1} + \frac{1 - v_2}{3\kappa_1}}}_{\kappa^{*,-}} \leq \kappa^* \leq \underbrace{\kappa_2 + \frac{1 - v_2}{\frac{1}{\kappa_1 - \kappa_2} + \frac{v_2}{3\kappa_2}}}_{\kappa^{*,+}}. \tag{27}$$

such that the effective parameter reads

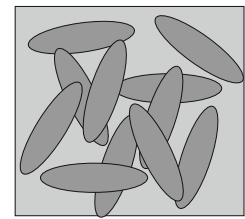
$$\kappa^* \approx \Psi \kappa^{*,+} + (1 - \Psi) \kappa^{*,-}. \tag{28}$$

In case of other material specific parameters, namely the mass density, the heat capacity, the susceptibilities, we use the volumetric fraction such that the microstructure effect is excluded

$$\rho^* = (1 - v_2) \rho_1 + v_2 \rho_2,$$



**PARTICLES WELL SEPARATED**  
 $\Psi < 1/2$



**PARTICLE TOUCHING**  
 $\Psi > 1/2$

**Fig. 2** Comparing microstructures with the same volume fractions. Flakes touch more, and thus need a higher value of  $\Psi$

$$\begin{aligned} c^* &= (1 - v_2)c_1 + v_2c_2, \\ \chi^* &= (1 - v_2)\chi_1 + v_2\chi_2. \end{aligned} \tag{29}$$

### 4.2 Nonlinearity due to the material parameters

As pointed out in the Introduction, the heat and electrical conductive material properties of all the materials depend on temperature and electric field. We assume for this dependence the following functional form:

$$\begin{aligned} \sigma &= \sigma_o \exp\left(-C_1 \frac{T - T_{ref.}}{T_{ref.}}\right) \exp\left(-C_2 \frac{\|E\| - E_{ref.}}{E_{ref.}}\right), \\ \kappa &= \kappa_o \exp\left(-C_3 \frac{T - T_{ref.}}{T_{ref.}}\right) \exp\left(-C_4 \frac{\|E\| - E_{ref.}}{E_{ref.}}\right), \end{aligned} \tag{30}$$

where  $C_x$  are material constants and  $T_{ref.}$ ,  $E_{ref.}$  are reference values. For  $T_{ref.}$  we can choose the initial temperature, where no flux or stress arise. For  $E_{ref.}$  we can choose the electric field at the breakdown voltage, at which the insulator becomes partially conductive. The constant  $\sigma_o$ ,  $\kappa_o$  is the value at the reference temperature and electric field. For the sake of simplicity we will use  $C_3 = C_4 = 0$  providing a constant thermal conductivity.

## 5 Results and comparison

By using the reduced model and FEM implementation, we solve the system shown in Fig. 1 out of four different materials for the equal set of boundary conditions. Since the conductivity of copper is high, there is a significant amount of production of entropy due to JOULE’s loss, increasing the temperature of the system (Fig. 2). For the reduced model we only solve in 1D and visualize in 3D by using the material coefficients compiled in Table 1.

In the case of FEM implementation, we embed the geometry in air as shown in Fig. 3.

**Table 1** Material coefficients for the reduced model

Material	Coefficient	Unit
Copper	$\rho = 8960$	kg/m <sup>3</sup>
	$\sigma_o = 5.8 \cdot 10^7$	S/m
	$C_1 = 1$	–
	$C_2 = 0$	–
	$\kappa = 400$	W/(mK)
	$c = 390$	J/(kg K)
Epoxy resin	$\rho = 1000$	kg/m <sup>3</sup>
	$\sigma_o = 1 \cdot 10^{-13}$	S/m
	$C_1 = 0$	–
	$C_2 = 10$	–
	$\kappa = 1.5$	W/(mK)
	$c = 800$	J/(kg K)
OCP	$E_{ref.} = 500 \cdot 10^6$	V/m
	$\rho^* = 1100$	kg/m <sup>3</sup>
	$\sigma_o^* = 10$	S/m
	$C_1 = 10$	–
	$C_2 = 10$	–
	$\kappa^* = 1$	W/(mK)
ECP	$c^* = 1000$	J/(kg K)
	$E_{ref.} = 20 \cdot 10^6$	V/m
	$\rho^* = 3000$	kg/m <sup>3</sup>
	$\sigma_o^* = 10^3$	S/m
	$C_1 = 10$	–
	$C_2 = 0$	–
	$\kappa^* = 10$	W/(mK)
	$c^* = 700$	J/(kg K)

**Table 2** Additional material coefficients for the FEM model

Material	Coefficient	Unit
Copper	$\chi^{el.} = 0$	–
	$\chi^{mag.} = -1 \cdot 10^{-5}$	–
	$\pi = 68 \cdot 10^{-6}$	V/K
Resin	$\chi^{el.} = 2$	–
	$\chi^{mag.} = 0$	–
	$\pi = 0$	V/K
OCP	$\chi_{el.}^* = 5$	–
	$\chi_{mag.}^* = 0$	–
	$\pi^* = 0$	V/K
ECP	$\chi_{el.}^* = 10$	–
	$\chi_{mag.}^* = 0$	–
	$\pi^* = 0$	V/K
Air	$\rho = 1.2$	kg/m <sup>3</sup>
	$\sigma_o = 3 \cdot 10^{-15}$	S/m
	$C_1 = 0$	–
	$C_2 = 0$	–
	$\kappa = 0.0257$	W/(mK)
	$c = 1005$	J/(kg K)
	$\chi_{el.} = 0$	–
	$\chi_{mag.} = 0$	–
	$\pi = 0$	V/K

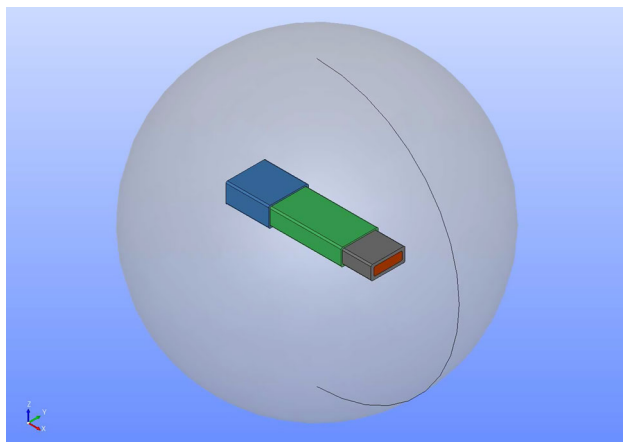


**Fig. 3** Power transmission cable model, copper as core (orange), resin as insulator (gray), OCP (green), and ECP (blue), all embedded in air (transparent). (Color figure online)

This 3D geometry allows us to set homogeneous far field boundaries, i.e., electromagnetic potentials vanish at

the outer shell. In addition to Table 1, we use the material parameters from Table 2.

All material constants are approximate but realistic values. The intention in this work is to test the proposed 1D model against 3D model quantitatively. In the 1D approach we obtain quick results because of several simplifications. One time step lasts approximately 1.5 s on a single core,<sup>1</sup> where most of the computation time is used for projecting on a 3D mesh for the sake of a better visualization. In the 3D model we involve many coupling effects and assume that the result is more accurate than the 1D approach. As expected, 3D modeling takes longer, for a time step approximately 17 min on 6 cores with the same machine. We perform a test example with both approaches and compare them in the following.

Consider a power station of  $P = 0.5$  MW where at the beginning of transmission the electric potential is converted to (a relatively low potential difference)  $V = 30$  kV at a standard frequency of 50 Hz. The conductor copper possesses the resistance  $R = V^2/P$  and the resistivity  $r = RA/L$ , where the cross-section  $A = A^I$  and the total length  $L = L^I + L^{II} + L^{III}$  are given. The electrical conductivity of copper is exchanged with  $\sigma_o = 1/r$  in order to model this phenomenon. In reality, there is an additional resistor restricting

<sup>1</sup> Intel Core i7-2600 at 3.4 GHz running on Ubuntu server with Linux 4.4.0-64-generic

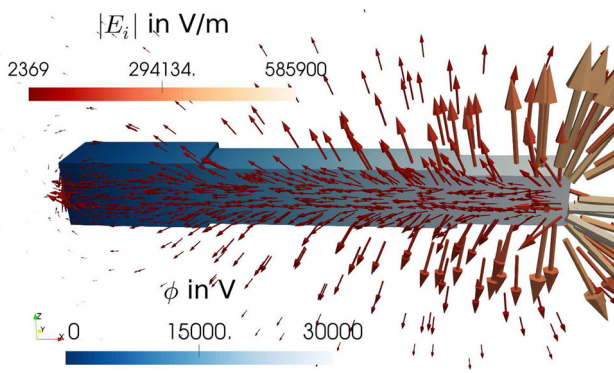


**Fig. 4** At the quarter of a cycle,  $t = 0.005$  s, distribution of electric potential (colors) and electric field (scaled arrows with colors) are shown. (Color figure online)

the electric current for the circuit. By applying the electric potential of 30 kV sinusoidally on one end and grounding the other end, we compute the electric potential and temperature directly, out of which the electric field and current are derived.

Since the loading is sinusoidal, we present in Fig. 4 the distribution of potential and electric field at the quarter of a cycle, where the amplitude 30 kV is reached.

The complete solution of electromagnetic potentials results in the expected characteristic closed (equipotential) lines. Within the conductor, the magnitude remains nearly constant and a comparison with the reduced model in Fig. 5 convinces us that the approximation of 1D model within the conductor has an error up to 4%.

It is important to recall that we use an effective conductivity in 1D model introduced in Eq. (7). For this specific example the approximation is accurate leading to a precise estimation of the electric current, too. Distribution of electric current and its comparison can be depicted in Fig. 6.

Since the electric potential is computed by using linear finite elements, its derivative leading to electric field and electric current is constant within each element. In the post-processing, however, the visualization smooths the fields such that apparent spikes are seen. The electric conductivity depends on the temperature, which is non-constant in 3D and constant in 1D across the cross-section. Therefore, there is a significant discrepancy between the computed magnitude—white arrows represent 3D computation, black arrow is the constant current from 1D model. However, the mean value of 3D solution matches the 1D electric current such that JOULE’s heat over the cross-section is nearly identical resulting to a similar temperature evolution, as seen in Fig. 7 at the end of a period.

We use discontinuous elements for presenting the 1D temperature solution such that the value has a sharp jump across the interface. In 3D model we use continuous elements and hence the interface is modeled depending on the mesh size.

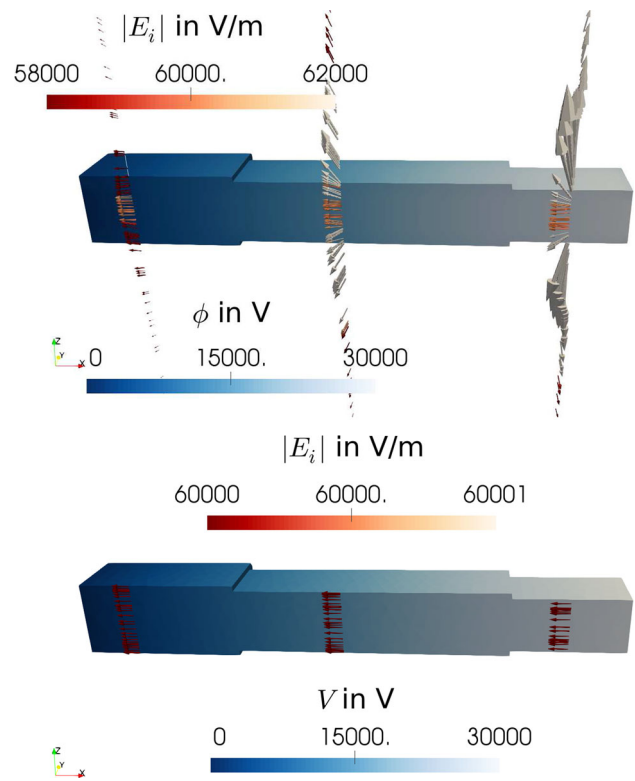


**Fig. 5** At the quarter cycle,  $t = 0.005$  s, electric potential distribution (colors), electric field from 3D model (top) as well as from 1D (bottom) with scaled and colored arrows on different slices are shown. (Color figure online)

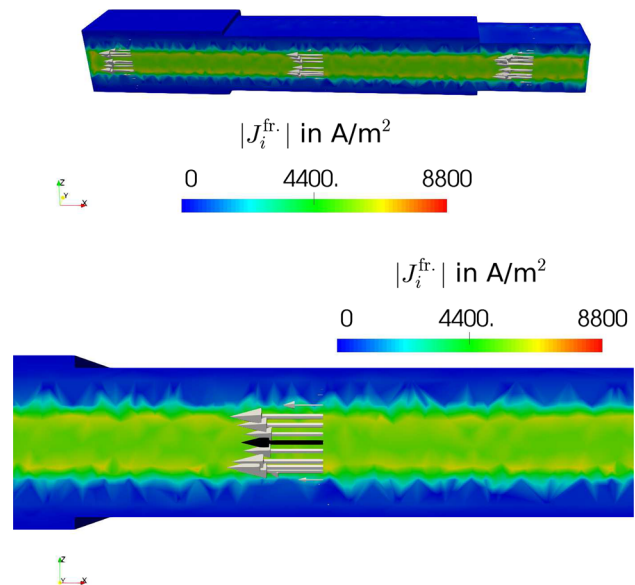


**Fig. 6** At the quarter cycle,  $t = 0.005$  s, electric current is shown. Top: magnitude in colors and scaled arrows in white from 3D model. Bottom: additionally 1D solution as black arrow (equally scaled) as representing the constant current along the cross-section

This phenomenon is indicated by using a cut on the element boundaries on  $y$ - $z$ -plane. The temperature difference to ini-

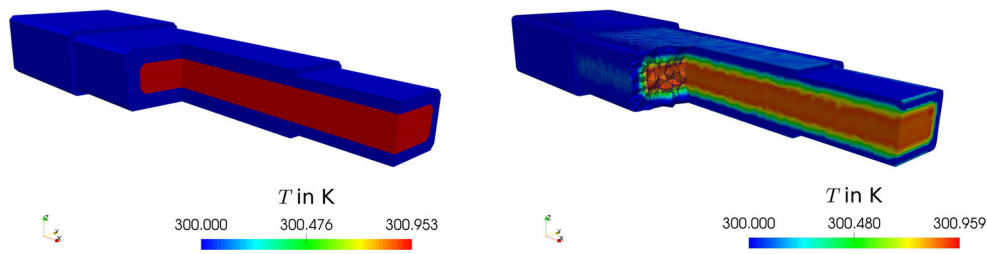


**Fig. 7** Temperature distribution obtained from 1D (left) and 3D (right) solutions, shown at the end of a loading cycle at 50 Hz, i.e.,  $t = 0.02$  s

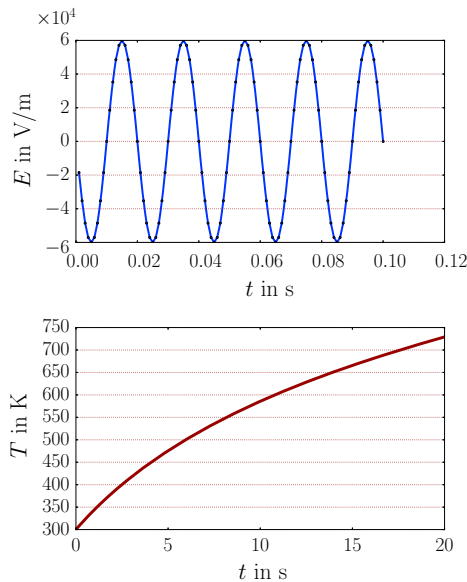


**Fig. 8** Temperature and electric field change over time under the excitation at 50 Hz. Top: electric field in 5 cycles. Bottom: temperature in 1000 cycles

tial  $T_{ref} = 300$  K is accurate within 1% error such that 1D model can be declared as verified for this specific application. In other words, the taken assumptions are admissible for the presented case. Polarization can be spared since the effective conductivity is approximating the electric potential distribution accurately. The weak coupling between the temperature and electric field is appropriate, because the instantaneous evolution of the electric field generates the same amount of heat over the whole conductor. Temperature conduction over the cross-section can be omitted as long as the cooling over the boundary becomes important for the application. In other words, we miss the effect of heat exchange with the environment. For studying the consequences, we perform another simulation only with the 1D model for 1000 cycles and present the electric field for the first 5 cycles and temperature over time in Fig. 8.

Even after 1000 cycles meaning 20 s, the temperature fails to reach a steady state. This phenomenon is indeed due to the lack of heat exchange in 1D model. Owing to the computational cost, 3D modeling is not feasible. For a concrete

application, a correction factor to JOULE’s heat—the system specific parameter  $a$  in Eq. (9)—can be introduced amending the temperature rise over time by simulating once with 3D model. For encouraging further studies, we make all codes publicly available in [1] to be used under the GNU Public license as written in [15].

## 6 Conclusion

In HV machines, corona discharge is seen as one of the main reasons of power losses. Efficient corona protection is of paramount importance and computational methods help to propose a new design or to amend existing designs. An electromagnetic simulation of part of a transmission is possible in 3D with all electrodynamics and coupling phenomena. However, such an analysis is computationally costly such that reduced-order models are used in the industry. We have developed a 1D model under several assumptions and verified their admissibility through a single run of a 3D model. The computed variables (electric potential and temperature) are compared, as well as the derived variables such as electric field, electric current are studied. The reduced-order model involving material nonlinearities performs an excellent estimation of the transient simulation for a very specific but realistic design. One deficiency and a possible correction is discussed. Codes are made publicly available for continuation of similar efforts for concrete geometries and conditions.

**Acknowledgements** T. Zohdi gratefully acknowledges the generous support of the Siemens corporation during the course of this research. B. E. Abali’s work was supported by a Grant from the Max Kade Foundation to the University of California, Berkeley.

## References

1. Abali BE (2016) Technical University of Berlin, Institute of Mechanics, Chair of Continuum Mechanics and Material Theory, Computational Reality. <http://www.lkm.tu-berlin.de/ComputationalReality>
2. Abali BE (2017) Computational reality, solving nonlinear and coupled problems in continuum mechanics. advanced structured materials. Springer, Berlin

3. Abali BE (2017) Computational study for reliability improvement of a circuit board. *Mech Adv Mater Mod Processes* 3(1):11
4. Abali BE, Reich FA (2017) Thermodynamically consistent derivation and computation of electro-thermo-mechanical systems for solid bodies. *Comput Methods Appl Mech Eng* 319:567–595
5. Arnold DN, Logg A (2014) Periodic table of the finite elements. *SIAM News* 47(9):212
6. Bossavit A (1988) Whitney forms: a class of finite elements for three-dimensional computations in electromagnetism. In: *IEEE Proceedings a physical science, measurement and instrumentation, management and education, reviews*, 135(8):493–500
7. Brockschmidt M, Gröppel P, Pohlmann F, Rohr C, Röding R (2013) Material for insulation system, insulation system, external corona shield and an electric machine, February 20 2013. US Patent App. 14/386,261
8. Chen G, Hao M, Xu Z, Vaughan A, Cao J, Wang H (2015) Review of high voltage direct current cables. *CSEE J Power Energy Syst* 1(2):9–21
9. Ciarlet P Jr, Zou J (1999) Fully discrete finite element approaches for time-dependent Maxwell's equations. *Numerische Mathematik* 82(2):193–219
10. Demkowicz L (2006) Computing with hp-adaptive finite elements: volume 1 one and two dimensional elliptic and Maxwell problems. CRC Press, Boca Raton
11. Donzel L, Greuter F, Christen T (2011) Nonlinear resistive electric field grading part 2: materials and applications. *IEEE Electr Insul Mag* 27(2):18–29
12. Egiziano L, Tucci V, Petrarca C, Vitelli M (1999) A galerkin model to study the field distribution in electrical components employing nonlinear stress grading materials. *IEEE Trans Dielectr Electr Insul* 6(6):765–773
13. Gatzsche M, Lücke N, Großmann S, Kufner T, Freudiger G (2017) Evaluation of electric-thermal performance of high-power contact systems with the voltage-temperature relation. *IEEE Trans Compon Packag Manuf Technol* 7(3):317–328
14. Gillette A, Rand A, Bajaj C (2016) Construction of scalar and vector finite element families on polygonal and polyhedral meshes. *Comput Methods Appl Math* 16(4):667–683
15. GNU Public. Gnu general public license. <http://www.gnu.org/copyleft/gpl.html>, June 2007
16. Hoffman J, Jansson J, Johnson C, Knepley M, Kirby RC, Logg A, Scott LR, Wells GN (2005) FEniCS. <http://www.fenicsproject.org>
17. Kelen A, Virsberg L-G (1962) Coating for equalizing the potential gradient along the surface of an electric insulation, November 27 1962. US Patent 3,066,180
18. Klausner B, Meyer C, Muhrer V, Maurer A, Russel C, Schafer K (2004) Corona shield, and method of making a corona shield, December 16 2004. US Patent App. 11/014,631
19. Li J (2009) Numerical convergence and physical fidelity analysis for Maxwell's equations in metamaterials. *Comput Methods Appl Mech Eng* 198(37):3161–3172
20. Logg A, Mardal KA, Wells GN (2011) Automated solution of differential equations by the finite element method, the FEniCS book, lecture notes in computational science and engineering, vol 84. Springer, Berlin
21. Meah K, Ula S (2007) Comparative evaluation of hvdc and hvac transmission systems. In: *Power engineering society general meeting, 2007*. IEEE, pp 1–5
22. Nédélec J-C (1980) Mixed finite elements in  $\mathbb{R}^3$ . *Numerische Mathematik* 35(3):315–341
23. Planas E, Andreu J, Gárate JI, de Alegría IM, Ibarra E (2015) AC and DC technology in microgrids: a review. *Renew Sustain Energy Rev* 43:726–749
24. Raviart P-A, Thomas J-M (1977) A mixed finite element method for 2-nd order elliptic problems. In: *Mathematical aspects of finite element methods*. Springer, pp 292–315
25. Schmidt G, Litinsky A, Staubach A (2015) Enhanced calculation and dimensioning of outer corona protection systems in large rotating machines. In: *International symposium on high voltage engineering*
26. Sharifi E, Jayaram S, Cherney EA (2010) A coupled electro-thermal study of the stress grading system of medium voltage motor coils when energized by repetitive fast pulses. In: *Conference record of the 2010 IEEE international symposium on electrical insulation (ISEI)*
27. Sima W, Espino-Cortes FP, Cherney EA, Jayaram SH (2004) Optimization of corona ring design for long-rod insulators using fem based computational analysis. In: *Conference record of the 2004 IEEE international symposium on electrical insulation, 2004*. IEEE, pp 480–483
28. Staubach C, Wulff J, Jenau F (2012) Particle swarm based simplex optimization implemented in a nonlinear, multiple-coupled finite-element-model for stress grading in generator end windings. In: *2012 13th international conference on optimization of electrical and electronic equipment (OPTIM)*. IEEE, pp 482–488
29. Stefanini D, Seifert JM, Clemens M, Weida D (2010) Three dimensional fem electrical field calculations for EHV composite insulator strings. In: *2010 IEEE international power modulator and high voltage conference (IPMHVC)*. IEEE, pp 238–242
30. Weida D, Böhmelt S, Clemens M (2010) Design of ZnO microvaristor end corona protection for electrical machines. In: *Conference record of the 2010 IEEE international symposium on electrical insulation (ISEI)*. IEEE, pp 1–4
31. Wheeler JCG, Gully AM, Baker AE, Perrot FA (2007) Thermal performance of stress grading systems for converter-fed motors. *IEEE Electr Insul Mag* 23(2):5–11
32. Zohdi TI (2012) *Electromagnetic properties of multiphase dielectrics: a primer on modeling, theory and computation*, vol 64. Springer, Berlin
33. Zohdi TI, Wriggers P (2008) *An introduction to computational micromechanics*, 2nd edn. Springer, Berlin
34. Zohdi TI (2017) Modeling and rapid simulation of the propagation and multiple branching of electrical discharges in gaseous atmospheres. *Comput Mech* 60(3):433–443
35. Zohdi TI, Monteiro PJM, Lamour V (2002) Extraction of elastic moduli from granular compacts. *Int J Fract* 115(3):49–54